Time evolution and finite element representation of Phase Space Zonal Structures in ORB5

Journal of Physics: Conference Series **2397** (2022) 012019 doi:10.1088/1742-6596/2397/1/012019

Time evolution and finite element representation of Phase Space Zonal Structures in ORB5

A. Bottino[1], M.V. Falessi[2], T. Hayward-Schneider[1], A. Biancalani[3], S. Briguglio[2], R. Hatzky[1], Ph. Lauber[1], A. Mishchenko[4], E. Poli[1], B. Rettino[1], F. Vannini[1], X. Wang[1], F. Zonca[2]

[1]Max-Planck-Institut für Plasmaphysik, 85748 Garching, Germany
[2]ENEA, Fusion and Nuclear Safety Department, 00044 Frascati (Roma), Italy
[3]Léonard de Vinci Pôle Universitaire, Research Center, 92916 Paris la Défense, France
[4]Max-Planck-Institut für Plasmaphysik, 17491 Greifswald, Germany

E-mail: alberto.bottino@ipp.mpg.de

Abstract. Phase Space Zonal Structures (PSZSs), obtained by averaging out dependencies on angle-like variables in the energetic particle (EP) distribution function, play a fundamental role in regulating EP transport induced by Alfvén instabilities in burning plasmas, acting as a slowly varying nonlinear equilibrium state. Therefore, they are of great interest for the development of reduced models for the description of EP heat and particle transport on long time scales, comparable with the energy confinement time, for future burning plasma experiments. In this work, we propose an efficient finite element based projection of the time evolution of the PSZS, suited for global particle-in-cell (PIC) gyrokinetic (GK) codes. The resulting algorithm has been implemented in the global GK PIC code ORB5. PSZSs can not only be used for validating reduced models, but also as a diagnostic tool for characterizing the nonlinear interaction in phase space between Alfvén instabilities and EPs in global GK simulations.

1. Introduction

Energetic particles (EPs) are crucial actors in the dynamics of magnetically confined burning plasmas. Such ions exhibit an average kinetic energy significantly higher then the thermal population. They are created by fusion reactions and they represent the key ingredient for heating magnetically confined plasmas at ignition. Energetic particles also appear in present day experiments as products of auxiliary heating sources such as neutral beam injection (NBI) or ion cyclotron resonance heating (ICRH). In Tokamaks, the typical EP velocity, v_{EP}, sits between the thermal bulk ion velocity $v_{\mathrm{th,i}}$ and the thermal electron velocity $v_{\mathrm{th,e}}$. Therefore, the EP characteristic dynamical frequencies, associated with their guiding-center motion (transit, bounce and precessional) are often comparable with the frequency of shear Alfvén waves (SAWs) (see, e.g., [1, 2]). Because of this, EPs can resonate with SAWs, driving them unstable. Alfvénic oscillations driven unstable by EPs are characterized by a broad spectrum of frequencies, since short wavelength kinetic SAWs can also be excited by resonant mode conversion. Quantitative predictions of the interplay between SAW instabilities and EPs require a kinetic treatment since resonances with ions substantially modify MHD predictions. Moreover, the nature of the nonlinearities in the kinetic equations leads to a direct wave-particle interaction and to kinetic corrections to the wave-wave interactions. Nonlinear gyrokinetic (GK) theory provides the

theoretical framework for calculating such interplay between SAWs and EPs and their impact on turbulent and collisional transport (see e.g. Refs. [3, 4]).
It has been shown that phase space structures, obtained by averaging out dependencies on angle-like variables in the energetic particle distribution function, which are not rapidly damped by collisionless processes such as Landau damping, play a fundamental role in regulating EP transport induced by Alfvén instabilities in burning plasmas (see Ref. [5] and references therein). These phase space structures are generally referred to as Phase Space Zonal Structures (PSZSs), by analogy with the meso-scale configuration space structures spontaneously generated by drift-wave turbulence; i.e., zonal flows and zonal fields. PSZSs act as a slowly evolving nonlinear plasma equilibrium. Recently, evolution equations for PSZSs have been derived from nonlinear GK theory [6, 5]. Those equations self-consistently describe the time evolution of PSZS, and consequently EP dynamics, up to transport time scales. Those equations are particularly important, since they allow the development of reduced transport models (see Ref. [7]) describing the evolution of macroscopic plasma profiles on long time scales [8], comparable with the energy confinement time, in burning plasma experiments [9]. Those kind of predictions are well beyond the actual capabilities of the existing global GK codes, despite the tremendous progress made in the last years (see e.g. Refs. [10, 11] for recent ORB5 reactor relevant simulations). Nevertheless, it is important to be able to compare the predictions of the time evolution of PSZSs with the results of existing GK code. In this work we propose an efficient finite element based projection of the time evolution of the PSZS, suited for global particle-in-cell (PIC) gyrokinetic codes. The resulting algorithm has been implemented in the global GK PIC code ORB5 [12]. PSZSs extracted from GK simulations can not only be used for validating reduced models, but also as a diagnostic tool for characterizing the nonlinear interaction in phase space between Alfvén instabilities. Note that similar diagnostics already exist in GK-hybrid codes, such as XHMGC [13, 14]. In addition to this, the information provided by the finite element projection of the distribution function could be used for significantly improving the quality of δf PIC simulations, by adjusting and updating the plasma reference state (background distribution function), during the nonlinear evolution of the system, consistently with PSZS dynamics.

2. Finite element representation of the PSZS

Following the definitions of [5, 6, 9], the PSZS is defined as the angle average (orbit average) of the gyrocenter distribution function

$$\hat{F}_{0,sp}(P_\varphi,\mu,\epsilon)=\tau_b^{-1}\oint\frac{\mathrm{d}\theta}{\dot{\theta}}F_{z,sp}\ ,\quad \tau_b=\oint\frac{\mathrm{d}\theta}{\dot{\theta}}\ ,\quad F_{z,sp}=\frac{1}{2\pi}\int_0^{2\pi}F_{sp}(P_\varphi,\mu,\epsilon,\theta,\varphi)\ \mathrm{d}\varphi\ , \tag{1}$$

with

$$\dot{\theta}=-\frac{v_\parallel}{eB^*_\parallel J_{\psi,\theta,\varphi}}\frac{\partial P_\varphi}{\partial\psi}\ ,\quad J^{-1}_{\psi,\theta,\varphi}=\nabla\varphi\cdot(\nabla\psi\times\nabla\theta)\ ,$$

where $Fsp(P_\varphi,\mu,\epsilon,\theta,\varphi)$ is the gyrocenter distribution function of the particle species sp, μ is the magnetic moment, $\epsilon=1/2(mv_\parallel^2+2\mu B)$ is the kinetic energy and

$$P_\varphi=m_{sp}v_\parallel\frac{T(\psi)}{q_{sp}B}+\psi\ , \tag{2}$$

is the toroidal canonical angular momentum, associated with the toroidal symmetry of an axisymmetric equilibrium magnetic field, defined by

$$\mathbf{B}=T(\psi)\nabla\varphi+\nabla\varphi\times\nabla\psi\ , \tag{3}$$

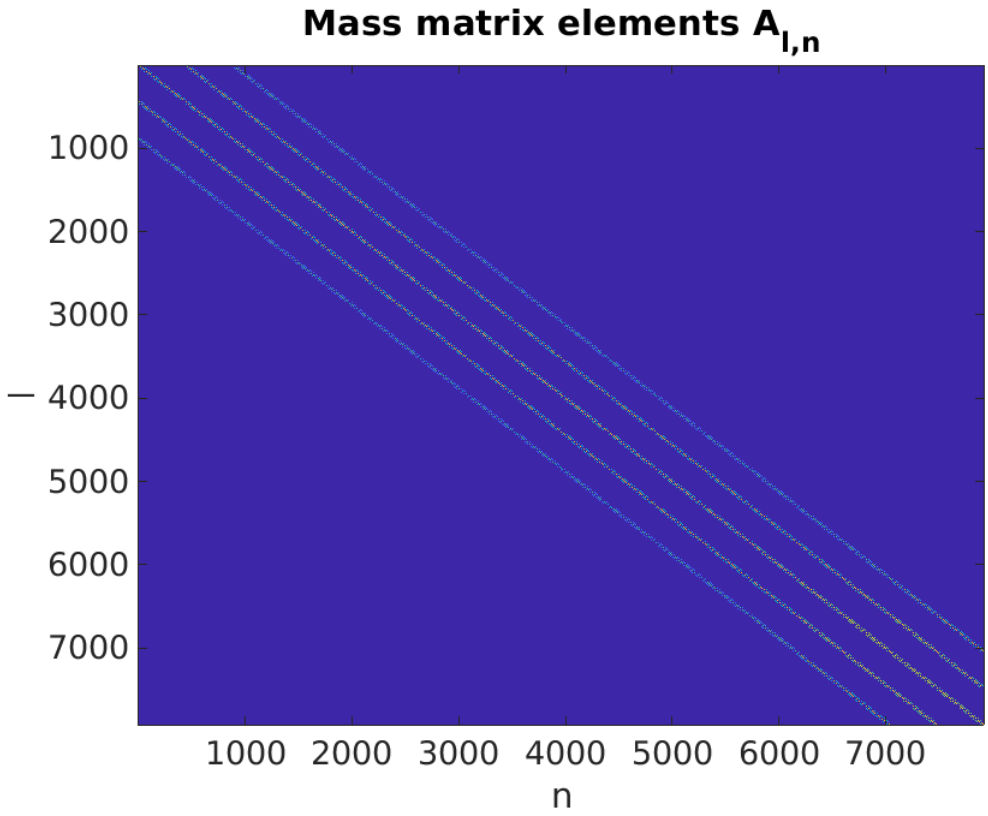

Figure 1: Mass matrix elements $A_{l,n}$, for a grid size ($N_{P\varphi} = 18, N_\epsilon = 16, N_\mu = 20$) and quadratic B-splines. The blue background corresponds to the zero elements of the matrix.

where ψ is the poloidal magnetic flux profile; m_{sp} and q_{sp} are mass and charge of the particle species sp, respectively. Note that both ϵ and P_φ are constants of motion on the unperturbed trajectories, while μ is an adiabatic invariant for the GK system of equations. Therefore, Eq. (1) can be interpreted, at a given time t and in a given phase-space position $(P_\varphi, \mu, \epsilon)$, as the average value of the distribution function on the unperturbed trajectories described by $(P_\varphi, \mu, \epsilon)$.
A finite element approximation of $\hat{F}_{0,sp}(P_\varphi, \mu, \epsilon)$ can be obtained by applying the Galerkin method (see e.g. [15]). The finite element representation of the PSZS is

$$\hat{F}_{0,sp}(P_\varphi, \mu, \epsilon, t) = \sum_l f_l(t)\Lambda_l(P_\varphi, \mu, \epsilon) \quad , \tag{4}$$

which is a linear combination of finite element basis functions (polynomia) Λ_l and $f_l(t)$ are time dependent real coefficients. For our discretisation, we choose B-splines as finite elements. Therefore, $\Lambda_l(P_\varphi, \mu, \epsilon)$ is actually the tensor product of three one dimensional B-splines of order d

$$\Lambda_l(P_\varphi, \mu, \epsilon) = \Lambda_i^d(P_\varphi)\Lambda_j^d(\epsilon)\Lambda_k^d(\mu) \ . \tag{5}$$

The sum over l is in fact a sum over 3 indices

$$\sum_l = \sum_{i=1}^{K_{P\varphi}} \sum_{j=1}^{K_\epsilon} \sum_{k=1}^{K_\mu} \ . \tag{6}$$

The number of polynomia considered in the sum is given, for each coordinate, by the number of (grid) points in which the domain is partitioned plus the order of polynomya considered,

i.e. $K_{P\varphi} = N_{P\varphi} + d$, $K_\epsilon = N_\epsilon + d$ and $K_\mu = N_\mu + d$.
A detailed description of B-splines can be found in Ref. [16].
The Galerkin method provides a general algorithm to calculate the spline coefficients $f_l(t)$ and it consists of 2 steps:

- Multiply equation (4) by a test function $g(P_\varphi, \mu, \epsilon) = \Lambda_n(P_\varphi, \mu, \epsilon)$
- Integrate the resulting equation over the space spanned by the basis functions.

Because of Eq. (4), we have:

$$\sum_l f_l(t) \int J(P_\varphi, \mu, \epsilon)\ \mathrm{d}P_\varphi\ \mathrm{d}\epsilon\ \mathrm{d}\mu\ \Lambda_n(P_\varphi, \mu, \epsilon)\Lambda_l(P_\varphi, \mu, \epsilon) = \int J(P_\varphi, \mu, \epsilon)\ \mathrm{d}P_\varphi\ \mathrm{d}\epsilon\ \mathrm{d}\mu\ \Lambda_n(P_\varphi, \mu, \epsilon)\hat{F}_{0,sp}(P_\varphi, \mu, \epsilon)\ , \quad (7)$$

where $J(P_\varphi, \mu, \epsilon)$ is the angle averaged Jacobian. The previous equation is actually a system of linear equations and it may be written in the more compact form as

$$\sum_l A_{l,n} f_l = b_n\ . \quad (8)$$

$A_{l,n}$ is the so called mass matrix, a 2D symmetric sparse band matrix with rank $(N_{P\varphi}+d)(N_\epsilon + d)(N_\mu + d)$. An example is given in Figure 1. Note that the angle average of the distribution function, needed to construct the PSZS, can be directly included in the calculation of b_n

$$b_n = \int \mathrm{d}P_\varphi\ \mathrm{d}\epsilon\ \mathrm{d}\mu\ \Lambda_n(P_\varphi, \epsilon, \mu) \left(\frac{1}{2\pi \int J(P_\varphi, \theta, \mu, \epsilon)\ \mathrm{d}\theta} \int J(P_\varphi, \theta, \mu, \epsilon)\ \mathrm{d}\theta\ \mathrm{d}\varphi\ F_{z,sp}(P_\varphi, \theta, \varphi, \epsilon, \mu) \right)\ . \quad (9)$$

The calculation of b_n is trivial if $F_{z,sp}(P_\varphi, \theta, \varphi, \epsilon, \mu)$ is analytically known or defined on a grid. In a PIC code, this projection is less trivial, as it will be discussed in the next section.

3. Implementation in ORB5

The code ORB5 [17, 18, 12] is based on a Monte Carlo Particle-in-Cell/Finite algorithm for discretising and solving the Gyrokinetic Vlasov-Maxwell system of equations. Altough ORB5 currently includes a multi-species, non-linear Coulomb collision operator [19], collision are not included in this work. The collisionless model solved in the code is rigorously derived from a gyrokinetic Lagrangian and it is described in detail in Ref. [20]. The gyrokinetic Lagrangian corresponding to the full electromagnetic ORB5 model is, in Hamiltonian formulation:

$$L = \sum_{sp} \int \mathrm{d}W\ \mathrm{d}V \Big(\big(e\mathbf{A} + p_\parallel \mathbf{b}\big) \cdot \dot{\mathbf{R}} + \frac{m_{sp}c}{q_{sp}} \mu\dot{\alpha} - H \Big) f_{sp} + \int \frac{|\nabla_\perp A_\parallel|^2}{8\pi} \mathrm{d}V\ \ , \quad (10)$$

$$H = \frac{p_{||}^2}{2m_{sp}} + \mu B + q_{sp} J_0 \left(\phi - \frac{p_{||}}{m_{sp}c} A_{||} \right) + \frac{q_{sp}^2}{2m_{sp}c^2} (J_0 A_{||})^2 - \frac{m_{sp}c^2}{2B^2} |\nabla_\perp \phi|^2\ \ ,$$

in which the coordinates are the gyrocenter position $\mathbf{R}$, the adiabatic invariant μ, the gyro angle α and the canonical parallel momentum $p_\parallel = m_{sp} v_\parallel + (q_{sp}/c) J_0 A_\parallel$, where $v_\parallel$ is the parallel velocity; $\mathrm{d}V$ and $\mathrm{d}W$ are the volume elements in physical and velocity space respectively. In the last expression $\mathbf{B}$ is the equilibrium magnetic field and ϕ is the perturbed electrostatic potential. $A_\parallel$ is the parallel component of the perturbed vector potential, J_0 is the gyro-average operator

and c is the speed of light. The particle gyrocenter trajectories are derived from the variational principles on the action and can be written in the following explicit form:

$$\begin{aligned}\dot{\mathbf{R}} &= \frac{1}{m_{sp}}\left(p_{\|}-\frac{q_{sp}}{c}J_0 A_{\|}\right)\frac{\mathbf{B}^*}{B^*_{\|}} \\ &+ \frac{c}{q_{sp}B^*_{\|}}\mathbf{b}\times\left[\mu\nabla B + q_{sp}\nabla J_0\big(\phi-\frac{p_{\|}}{m_{sp}c}A_{\|}\big)\right] \ , \end{aligned} \tag{11}$$

$$\dot{p_{\|}} = -\frac{\mathbf{B}^*}{B^*_{\|}}\cdot\left[\mu\nabla B + e\nabla J_0\big(\phi-\frac{p_{\|}}{m_{sp}c}A_{\|}\big)\right] \ , \tag{12}$$

where $\mathbf{B}^* = \nabla\times\mathbf{A}^*$, $\mathbf{A}^* \equiv \mathbf{A} + (p_{\|}/q_{sp})\mathbf{b}$ and $\mathbf{b} = \mathbf{B}/B$. The distribution function is split into a constant in time background, $F_{0,sp}$, and a fluctuating part δF_{sp}. Only the time varying part of the distribution function, δF_{sp}, is discretized using Monte Carlo markers and it is evolved (in the absence of sources and collisions) according to the GK Vlasov equation:

$$\frac{\mathrm{d}\delta F_{sp}}{\mathrm{d}t} = -\frac{\partial F_{0,sp}}{\partial\mathbf{R}}\cdot\dot{\mathbf{R}} - \frac{\partial F_{0,sp}}{\partial p_{\|}}\dot{p_{\|}} = 0 \ . \tag{13}$$

Energy and momentum conservation can be proved via gyrokinetic field theory [20]. To self-consistently evolve the perturbed electrostatic and magnetic potentials, the Vlasov equation should be coupled with equations for the fields. Those are obtained by taking functional derivatives of the action functional with respect the perturbed potential, leading to a polarization equation for ϕ and Ampère's law for $A_{||}$. In this work we have used the electrostatic limit of the model and adiabatic electrons. The corresponding equations are obtained by setting $A_{\|} = 0$ in the previous equations and by assuming a fluid like response of the electrons density to the potential perturbation. The full derivation and discretisation of the electrostatic model can be found in reference [21]. In general, the electromagnetic equations are solved in ORB5 in the mixed-variable formulation of the GK equations and solved using the mixed-variable pullback algorithm [22]. In the code, a set of straight field line coordinates (s,θ^*,φ) is used, with $s=\sqrt{\psi/\psi_{\mathrm{edge}}}$, where ψ is the poloidal magnetic flux, and θ^* is the magnetic poloidal angle

$$\theta^* = \frac{1}{q(s)}\int^{\theta}\frac{B\cdot\nabla\varphi}{B\cdot\nabla\theta'}d\theta' \tag{14}$$

where θ is the geometric poloidal angle, φ the toroidal angle and $q(s)$ is the safety factor.
In ORB5 the perturbed distribution function is discretised using N markers

$$\delta F \simeq \frac{N_{\mathrm{ph}}}{N}\sum_{p=1}^{N}\frac{1}{2\pi B^*_{\|}}\delta w_p(t)\delta\big(\mathbf{R}-\mathbf{R}_p(t)\big)\delta\big(v_{\|}-v_{\|p}(t)\big)\delta\big(\mu-\mu_p(t_0)\big) \ , \tag{15}$$

where N_{ph} is the number of *physical* particles, i.e. $N_{\mathrm{ph}} = \overline{n}V$ where $\overline{n}$ is the volume averaged particle density and V is the volume of the torus. Each marker is characterized by a weight $\delta w_p(t)$ and by its (randomly chosen) location in phase-space, $(\mathbf{R}_p(t), v_{\|p}(t), \mu_p(t_0))$, where the magnetic moment is an adiabatic invariant for the gyrokinetic Lagrangian.
The marker weight is often interpreted as the (possibly normalized) value of the distribution function at the particle position. Actually, the meaning of the particle weights becomes apparent

by integrating Eq. (15) over the full phase-space volume Ω :

$$\begin{aligned}\int_\Omega \mathrm{d}^3R\ \mathrm{d}^3v\ \delta F &= \overline{\delta F}_\Omega \Omega \qquad (16)\\ &\simeq \int_\Omega \mathrm{d}^3R\ \mathrm{d}^3v\ \frac{N_{\mathrm{ph}}}{N}\sum_{p=1}^{N}\frac{1}{2\pi B_\parallel^*}\delta w_p(t)\delta\big(\mathbf{R}(t)-\mathbf{R}_p\big)\delta\big(v_\parallel(t)-v_{\parallel p}\big)\delta\big(\mu(t_0)-\mu_p\big)\ ,\end{aligned}$$

where $\overline{\delta F}_\Omega$ represents the average value of the number density perturbation over the phase-space volume Ω. Note that:

$$\mathrm{d}^3R\ \mathrm{d}^3v = J(R,Z)B_\parallel^*\ \mathrm{d}R\ \mathrm{d}Z\ \mathrm{d}\varphi\ \mathrm{d}v_\parallel\ \mathrm{d}\mu\ \mathrm{d}\alpha\ , \qquad (17)$$

which motivates the inclusion of the $2\pi B_\parallel^*$ factor in Eq. (15).
In particular, we could choose a set of N volumes Ω_p, each one centered around a single marker position $(\mathbf{R}_p, v_{\parallel p}, \mu_p)$ and for which $\sum_{p=1}^{N}\Omega_p = \Omega$, without overlapping.
We then use the properties of the δ functions and the fact that only a single marker would contribute to the integral, to solve the integral on the left-hand-side of Eq. (16):

$$\begin{aligned}\overline{\delta F}_p\Omega_p &= \int_{\Omega_p}\mathrm{d}^3R\ \mathrm{d}^2v\ \frac{N_{\mathrm{ph}}}{N}\frac{1}{B_\parallel^*}\delta w_p(t)\delta\big(\mathbf{R}-\mathbf{R}_p(t)\big)\delta\big(v_\parallel - v_{\parallel,p}(t)\big)\delta\big(\mu-\mu_p(t_0)\big)\\ &= \frac{N_{\mathrm{ph}}}{N}\delta w_p(t)\ , \qquad (18)\end{aligned}$$

where $\overline{\delta F}_p$ represents the average value of the number density perturbation over the phase-space volume Ω_p and $\mathrm{d}^2v = \mathrm{d}v_\parallel\ \mathrm{d}\mu$. Therefore, Ω_p can now be identified as the portion of phase-space volume described by the marker p and the weight δw_p as the average variation in number of particles on the volume Ω_p, up to normalization factors. The Liouville theorem guarantees that the value of Ω_p is conserved along the Lagrangian trajectories. Moreover, given that at $t = 0$ the phase-space marker position, $(\mathbf{R}_p, v_{\parallel p}, \mu_p)$, is located inside the volume Ω_p, it will stay inside that volume during the entire time evolution. However, the shape of the volume Ω_p will change in time (filamentation) possibly leading to a decrease of accuracy in the discretization, i.e. the numerical error associated to the PIC discretization of Eq. (15) will increase in time.
Here, the important information is that the actual value of the weight does not depend on the coordinate system in which the marker position is evolved, but only on the choice of the volume Ω_p associated to each marker.
If another set of coordinates was used, for example $(P_\varphi, \theta, \varphi, \epsilon, \mu)$, Eq.(18) would become

$$\begin{aligned}\overline{\delta F}_p\Omega_p = \int_{\Omega_p}\hat{J}\ \mathrm{d}\theta\ \mathrm{d}\varphi\ \mathrm{d}P_\varphi\ \mathrm{d}\epsilon\ \mathrm{d}\mu\ \frac{N_{\mathrm{ph}}}{N}\frac{1}{\hat{J}}\delta w_p(t)\delta\big(P_\varphi - P_{\varphi,p}(t)\big)\\ \delta\big(\theta-\theta_p(t)\big)\delta\big(\varphi-\varphi_p(t)\big)\delta\big(\epsilon-\epsilon_p(t)\big)\delta\big(\mu-\mu_p(t_0)\big) = \frac{N_{\mathrm{ph}}}{N}\delta w_p(t)\ , \qquad (19)\end{aligned}$$

i.e., only the details of the Jacobian $\hat{J}$ in the integral and in Eq. (15) would change, but the meaning of the weights does not change. In summary, the information carried by each marker weight is related to how many physical particles are contained into each volume Ω_p and it is independent of the system of coordinates chosen. Therefore, in a PIC code like ORB5, any integral (moment) of the distribution function is approximated by a sum on the (normalized) weights and Eq. (16) becomes:

$$\int_\Omega \mathrm{d}^3R\ \mathrm{d}^2v\ \delta F_{sp} \simeq \sum_{p=1}^{N}\overline{\delta F}_p\Omega_p = \frac{N_{\mathrm{ph}}}{N}\sum_{p=1}^{N}\delta w_p\ . \qquad (20)$$

The weights are renormalized at $t = 0$ in ORB5 by redefining them as

$$\overline{\delta w}_p = \delta w_p - \frac{1}{N}\sum_{p=1}^{N} \delta w_p \ , \tag{21}$$

in order to guarantee the requirement

$$\int_\Omega \mathrm{d}^3R \ \mathrm{d}^2v \ \delta F_{sp} = 0 \ . \tag{22}$$

For a full-f PIC code, the integral of F_{sp} would be

$$N_{\mathrm{p}h} = \int_\Omega \mathrm{d}^3R \ \mathrm{d}^2v \ F_{sp} \ \simeq \ \sum_{p=1}^{N} \overline{F}_p \Omega_p = \frac{N_{\mathrm{ph}}}{N}\sum_{p=1}^{N} w_p \ , \tag{23}$$

and the (time independent) full weights w_p would have to satisfy the property

$$\frac{1}{N}\sum_{p=1}^{N} w_p = 1 \ . \tag{24}$$

In ORB5 any integral of the full distribution function F_{sp} is the sum of two contributions

$$\int_\Omega \mathrm{d}^3R \ \mathrm{d}^2v \ F_{sp} \ \simeq \ \sum_{p=1}^{N} \overline{F}_p \Omega_p = \sum_{p=1}^{N} \left(\frac{N_{\mathrm{ph}}}{N} \overline{\delta w}_p + F_{0,sp}(\mathbf{R}_p, v_{\parallel p}, \mu_p)\Omega_p \right) \ , \tag{25}$$

where all the coordinates with a subscript p are evaluated at the marker position.
The same result can be obtained in a rigorous way by writing the integral of the left-hand-side of Eq. (16) using Monte carlo theory, i.e. as an expected value, $E[X]$, of a random variable X, with respect to a probability density $g(\mathbf{x})$. Here $\mathbf{x}$ represents a continuous 5D variable of components $(\mathbf{R}, v_\parallel, \mu)$. The general derivation can be found in Section 2 of Ref. [23]. Therefore, there is a direct connection between the phase-space volumes Ω_p and the probability density $g(\mathbf{x})$. This can be seen by rewriting the integral of Eq. (16) as

$$\int_\Omega F(\mathbf{x}) \ \mathrm{d}\mathbf{x} \ = \ \int_\Omega \frac{F(\mathbf{x})}{g(\mathbf{x})} g(\mathbf{x}) \ \mathrm{d}\mathbf{x} = E[X] \ \text{ with } \ X(\mathbf{x}) = \frac{F(\mathbf{x})}{g(\mathbf{x})} \ . \tag{26}$$

Following Ref. [23], the expected value $E[X]$ is approximated by an unbiased Monte Carlo estimator, based on an independent random sample $(\mathbf{x}_1, ..\mathbf{x}_i, ..\mathbf{x}_N)$ of N Monte Carlo sampling points (markers) with $\mathbf{x}_i \in \Omega$

$$E[X] \ \simeq \ \frac{1}{N}\sum_{p=1}^{N} \tilde{w}_p \ \text{ with } \ \tilde{w}_p = \frac{F(\mathbf{x}_p)}{g(\mathbf{x}_p)}. \tag{27}$$

In Monte Carlo theory, $\tilde{w}_p$ is often called *likelihood ratio* or *importance sampling ratio*. The similarities between Eq. (23) and Eq. (27) clearly show that the PIC algorithm is strongly related to the Monte Carlo integral method. In particular, it can be shown that the value of phase-space volume Ω_p is inversely proportional to the probability density $g(\mathbf{x})$ at the marker position. Note that, while the expected value is independent on the details of the probability density, the choice of $g(\mathbf{x})$ (and consequently of Ω_p) strongly influences the statistical noise in

PIC simulations [23].
Using those results, the projection of the PSZS on the B-splines, i.e. the calculation of the left-hand-side of the matrix problem given by Eq. (9), becomes

$$b_n = \sum_{p=1}^{N} \left(\frac{N_{\mathrm{ph}}}{N} \overline{\delta w}_p + f_0(P_{\varphi,p}, \theta_p, \epsilon_p, \mu_p) \Omega_p \right) \Lambda_n(P_{\varphi,p}, \epsilon_p, \mu_p) \ . \tag{28}$$

The B-spline solver of ORB5 has been adapted to a 3D non periodic matrix problem and extended to an arbitrary order of B-splines. The mass matrix is stored in an upper-band format. In the present version of the code, a direct serial solver based on Cholesky decomposition is used, which is fast but memory consuming. Therefore, in production runs the b_n coefficients are computed during the execution and stored in a HDF5 file. The mass matrix is reconstructed and factorized in a separate code and the linear problem of Eq. (8) is solved offline. In general, B-splines of order $d = 1$ (linear) appear to be accurate enough for most of the cases studied. However, higher order B-splines have the useful property of providing also the derivatives of the discretized function, without any additional numerical cost. Therefore, B-splines of order 2 are typically used for the PSZS in ORB5 production runs. Note that the resulting code has been extensively tested with analytical distribution functions, simplified geometries and reduced dimensionality. However, instead of discussing those verification tests, we prefer here to focus on the application of the newly developed diagnostics to an experimentally relevant and well documented scenario.

4. Numerical results

All the simulations presented in this Section are base on the so called NLED-AUG case [24]. This scenario corresponds to the magnetic equilibrium and profiles measured at $t = 0.84$ s in the discharge number 31213 performed in the ASDEX Upgrade (AUG) Tokamak. This experimental case is particularly relevant for EP physics. In particular the NBI generated fast-ions exhibit an MHD β (ratio of the plasma pressure to magnetic pressure) comparable to that of the bulk plasma, while the EP average kinetic energy is approximately 100 times higher than the bulk species temperature, comparable to the expected ratios of plasma parameters that are going to be met in future fusion machines such as ITER and DEMO. In this scenario, an intense EP-driven activity is observed, the stabilizing effects of the bulk plasma being minimized. The NLED-AUG case has been widely studied and simulated by several codes, including ORB5 [25, 26, 27, 28]. Moreover, it has also been used as benchmark case for GK and MHD/Hybrid codes [29]. Energetic particles are simulated using an analytical equilibrium distribution function corresponding to a pitch-angle dependent slowing down function (see Eq. (3) of [27]). For such a distribution function, EPs can excite an energetic-particle driven geodesic acoustic mode (EGAM) via inverse Landau damping with the resonant EPs, which causes a redistribution of the EPs in phase space from higher to lower energies. EGAMs are indeed present in the experimental measurement of the NLED-AUG case. In Ref. [27] the effects of such distributions on the stability of EGAMs on the NLED-AUG case have been studied in detail. In particular, the stability threshold values have been obtained as a function of the injection pitch angle $\xi_0 = v_\parallel/|v|$, the width of the non-isotropic (Gaussian) component of the distribution function σ_ξ and the EP concentration $n_{\mathrm{EP}}/n_{\mathrm{e}}$, n_{e} being the (volume integrated) electron density. In the following, $\xi_0 = -0.5$, $\sigma_\xi = 0.2$ and $n_{\mathrm{EP}}/n_{\mathrm{e}} = 0.0949$ are used, corresponding to a clearly unstable EGAM. The only difference as compared to the simulations discussed in Ref. [27] is that here nonlinear terms are kept in the particle equations of motion.

As a first test, we have constructed an angle averaged projection of the distribution function as a function of the original dynamical variables of ORB5 $(\psi, v_\parallel, \mu)$. With this choice of coordinates, the angle average is equivalent to a flux surface average. Practically, the same

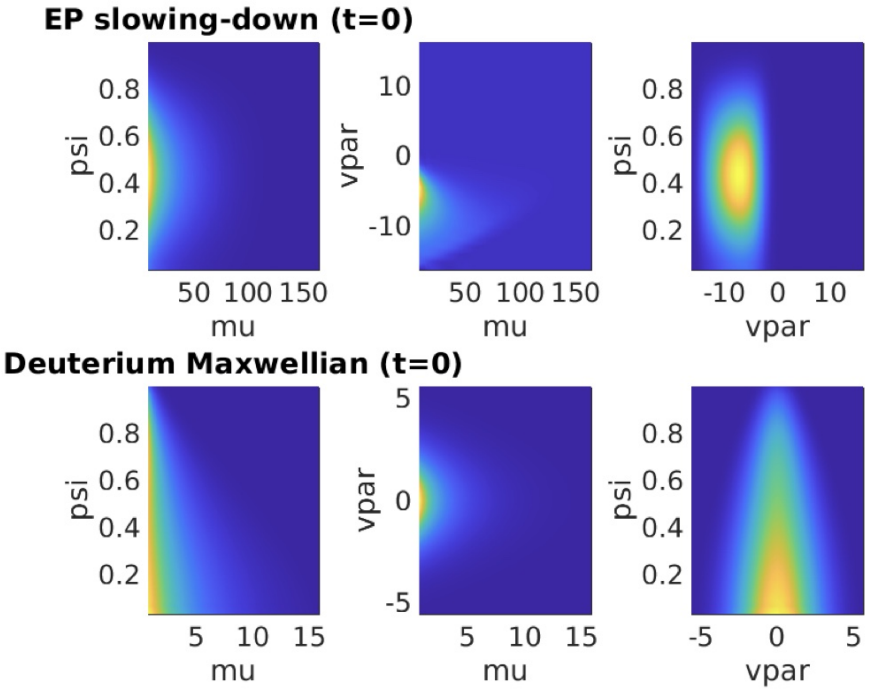

Figure 2: 2D projection of the angle averaged distribution function of EPs and bulk ions (Deuterium), using the PSZS numerical infrastructure, at $t = 0$, for the NLED-AUG case, for $(N_\psi = 30, N_\mu = 30, N_{v\|} = 30)$ and $d = 1$. The axis labels are psi $= \psi$, vpar $= \mathrm{v}_\|$ and mu $= \mu$.

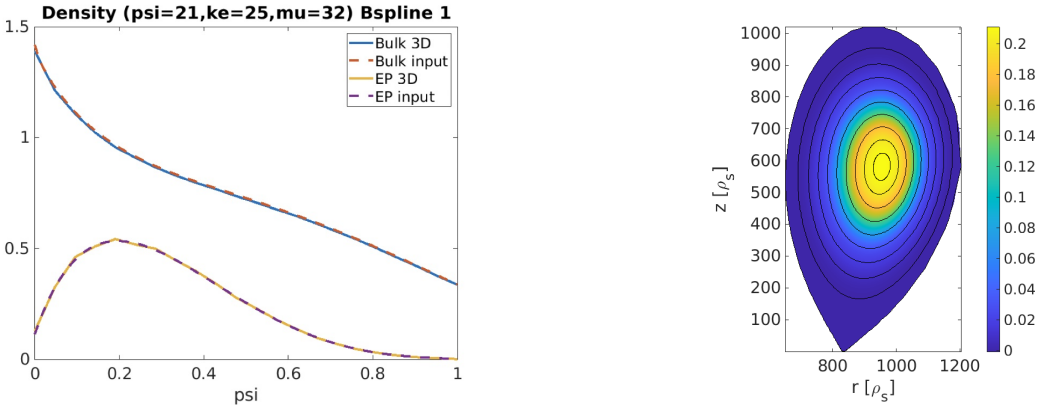

(a) (b)

Figure 3: (a) Comparison between the analytical and the reconstructed density using the PSZS data, for the NLED-AUG case, for $(N_\psi = 30, N_\mu = 30, N_{v\|} = 30)$ and $d = 1$. The x axis label is psi $= \psi/\psi$edge. (b) Poloidal cross section of the electrostatic potential during the linear phase, at $t = 2 \cdot 10^3$ $[\Omega_c^{-1}]$, solid black lines correspond to constant $\sqrt{\psi}$ magnetic surfaces. Labels are given in unit of the ion sound Larmor radius ρ_s on axis $(\psi = 0)$.

numerical infrastructure of the PSZS diagnostics is used, with the only difference of using a

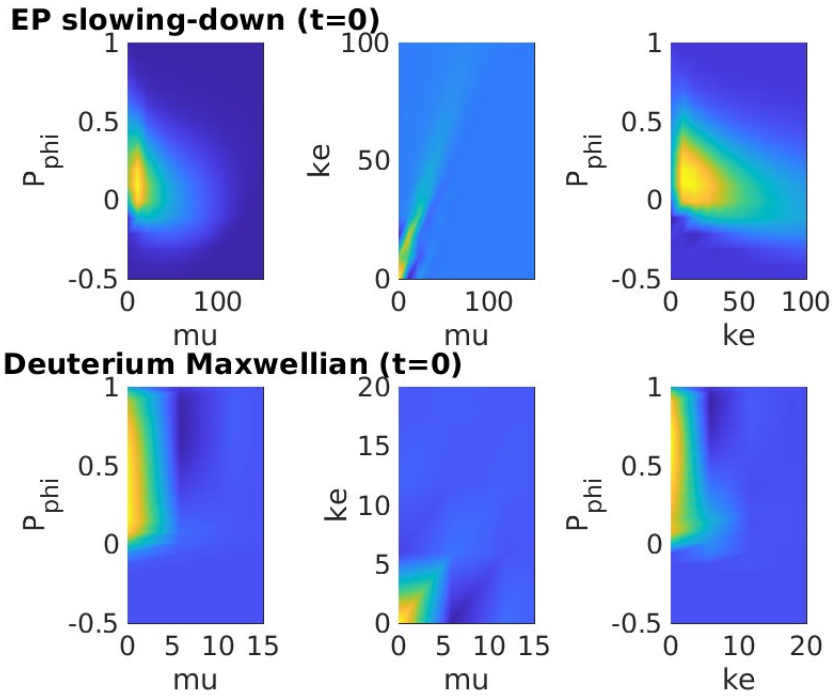

Figure 4: 2D projection of PSZS at $t = 0$, for the NLED-AUG case, for ($N_{P\varphi} = 30, N_\mu = 30, N_\epsilon = 30$) and $d = 1$. The axis labels are $\mathrm{P_{phi}} = \mathrm{P}_\varphi$, ke $= \epsilon$ and mu $= \mu$.

B-spline basis projection on the original variables,

$$\hat{F}_{0,sp}(\psi, \mu, v_\parallel) = \sum_l f_l(t)\Lambda_l(\psi, \mu, v_\parallel) \quad , \tag{29}$$

and consistently adapt the matrix construction and the calculation of the b_l vector. The result at $t = 0$ is shown in Fig. 2. Note that each plot of Fig. 2 corresponds to a 2D projection of the 3D data obtained by integrating on the third direction. At $t = 0$ only the background distribution function contributes to the projection. Therefore, this allows for a direct comparison between the PSZS diagnostics (which is a markers based quantity) and the analytical functions directly coded into ORB5. A particularly useful test consists in calculating the integral of the PSZS at $t = 0$ on the two velocity space coordinates, which should lead to exactly the same density profile provided as input into ORB5. The result is shown in Fig. 3(a). The good match between the input profile and the reconstructed density for both EPs and Maxwellian bulk ions also assures that the phase-space geometry is properly taken into account in the B-spline projection, even for an experimentally reconstructed magnetic equilibrium. The magnetic surfaces (as ($\sqrt{\psi}$ contours) for the NLED-AUG case are shown as solid lines in Fig. 3(b).
Figure 4 shows the results of the PSZS diagnostics, $\hat{F}_{0,sp}(P_\varphi, \mu, \epsilon)$, at $t = 0$ for the same case. Note that in both simulations the number of grid points used for the B-spline projection was fixed to ($N_{P\phi} = N_\psi = 30, N_\mu = 30, N_\epsilon = N_{v\parallel} = 30$). During the time evolution, an unstable EGAM appears close to the plasma center. This is clearly visible in Fig. 3(b), where the electrostatic potential is plotted during the linear phase, at $t = 2 \cdot 10^3$ [Ω_c^{-1}], Ω_c being the ion cyclotron frequency at B_0. In order to emphasize the corrugations in phase-space of $\hat{F}_{0,sp}(P_\varphi, \mu, \epsilon)$, in Fig. 5 only the δF component of the PSZS is plotted at $t = 2.6 \cdot 10^4$ [Ω_c^{-1}] (nonlinear phase). The modification in phase-space of the EP distribution function due to the interaction of the EGAM

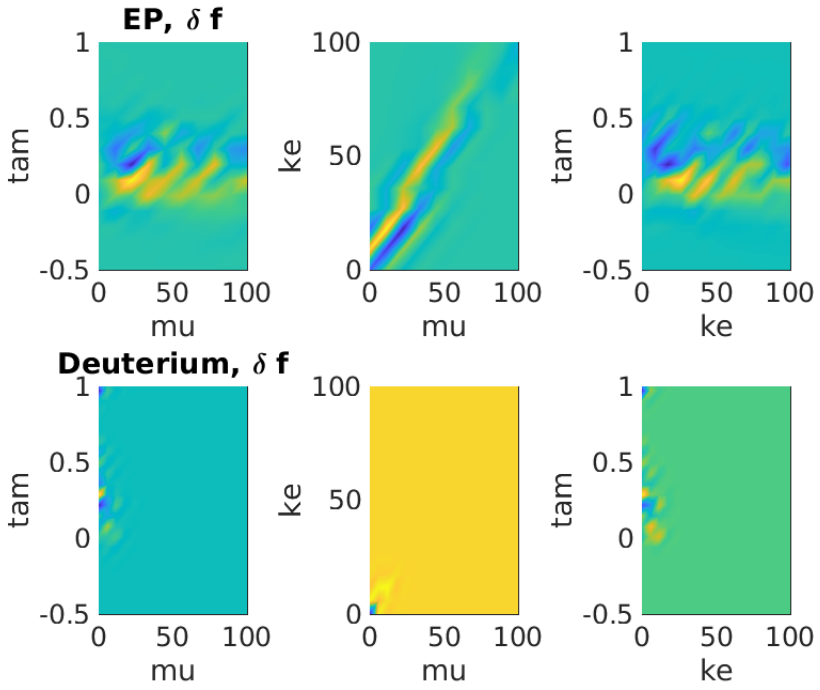

Figure 5: 2D projection of PSZS at $t = 2.6 \cdot 10^4 [\Omega_c^{-1}]$, for the NLED-AUG case, for ($N_{P\varphi} = 30, N_\mu = 30, N_\epsilon = 30$) and $d = 1$. The axis labels are $\mathrm{P_{phi}} = \mathrm{P}_\varphi$, ke $= \epsilon$ and mu $= \mu$; velocities are given in units of the sound velocity at mid radius.

and EPs is clearly visible in all the 2D projections of the 3D PSZS diagnostics. As expected, no significant modification to the bulk ion (Deuterium) distribution function is detected by the PSZS diagnostics.

5. Conclusions and discussion

A direct calculation of the PSZS, i.e. the slowly varying component of the distribution function averaged over the angle-like variables, has been implemented in ORB5, via a finite-element representation on 3D B-spline polynomia. The run-time algorithm is in general very fast since only one additional loop is required on the markers, which are usually partitioned among thousands of cores. For the largest case run so far, corresponding to ($N_{P\phi} = 80, N_\mu = 80, N_\epsilon = 80$) and cubic B-splines ($d = 3$), the overhead on the single time step, in which the PSZS was calculated, was less then 10% as compared to the original code. The PSZS is usually not calculated at every time step. The typical diagnostics frequency varies between 10 and 100 time steps, depending on the numerical and physics requirements. Therefore, its impact on the code performance on production runs is negligible. On the other hand, the post processing, i.e. the matrix construction, factorization and the back solve operations can be rather slow. For example, the post processing of the ($N_{P\phi} = 80, N_\mu = 80, N_\epsilon = 80$) case mentioned above took almost 4 hours on an Intel Xeon IceLake node with 256 GB RAM. In this specific case, around 600 PSZS data points were acquired, for each of the three kinetic species (Bulk ions, EPs and electrons) simulated. Note that in the present version of the post processing code, neither the matrix construction nor the backsolve are parallelized. Moreover, while ORB5 can run on GPU, the present version of the PSZS online and offline code can be used on CPUs only.

Acknowledgments
This work has been carried out within the framework of the EUROfusion Consortium, funded by the European Union via the Euratom Research and Training Programme (Grant Agreement No 101052200 – EUROfusion). Views and opinions expressed are however those of the authors only and do not necessarily reflect those of the European Union or the European Commission. Neither the European Union nor the European Commission can be held responsible for them. Part of the simulations discussed in this work were performed on the MARCONI FUSION HPC system at CINECA.

References

[1] Chen L and Zonca F 2007 *Nuclear Fusion* **47** S727–S734 URL https://doi.org/10.1088/0029-5515/47/10/s20
[2] Lauber P 2013 *Physics Reports* **533** 33–68 ISSN 0370-1573 URL https://www.sciencedirect.com/science/article/pii/S0370157313002676
[3] Chen L and Zonca F 2016 *Rev. Mod. Phys.* **88** 015008
[4] Sugama H 2017 *Rev. Mod. Phys.* **1** 9
[5] Falessi M V and Zonca F 2019 *Physics of Plasmas* **26** 022305 (*Preprint* https://doi.org/10.1063/1.5063874) URL https://doi.org/10.1063/1.5063874
[6] Zonca F, Chen L, Briguglio S, Fogaccia G, Vlad G and Wang X 2015 *New Journal of Physics* **17** 013052 URL https://doi.org/10.1088/1367-2630/17/1/013052
[7] Eurofusion ENR ATEP Project, (2021) https://wiki.euro-fusion.org/wiki/Project_No10
[8] Falessi M V and Zonca F 2018 *Physics of Plasmas* **25** 032306 (*Preprint* https://doi.org/10.1063/1.5018175) URL https://doi.org/10.1063/1.5018175
[9] Zonca F, Chen L, Falessi M V and Qiu Z 2021 *Journal of Physics: Conference Series* **1785** 012005 URL https://doi.org/10.1088/1742-6596/1785/1/012005
[10] Mishchenko A, Bottino A, Hayward-Schneider T, Poli E, Wang X, Kleiber R, Borchardt M, Nührenberg C, Biancalani A, Könies A, Lanti E, Lauber P, Hatzky R, Vannini F, Villard L and Widmer F 2022 *Plasma Physics and Controlled Fusion* **64** 104009 URL https://doi.org/10.1088/1361-6587/ac8dbc
[11] Hayward-Schneider T, Lauber P, Bottino A and Mishchenko A 2022 *Nuclear Fusion* URL http://iopscience.iop.org/article/10.1088/1741-4326/ac6f12
[12] Lanti E, Ohana N, Tronko N, Hayward-Schneider T, Bottino A, McMillan B F, Mishchenko A, Scheinberg A, Biancalani A, Angelino P, Brunner S, Dominski J, Donnel P, Gheller C, Hatzky R, Jocksch A, Jolliet S, Lu Z X, Collar J P M, Novikau I, Sonnendruecker E, Vernay T and Villard L 2020 *COMPUTER PHYSICS COMMUNICATIONS* **251** ISSN 0010-4655
[13] Briguglio S, Fogaccia G, Vlad G, Zonca F, Shinohara K, Ishikawa M and Takechi M 2007 *Physics of Plasmas* **14** 055904 (*Preprint* https://doi.org/10.1063/1.2710208) URL https://doi.org/10.1063/1.2710208
[14] Wang X, Briguglio S, Di Troia C, Falessi M V, Fogaccia G, Fusco V, Vlad G and Zonca F 2022 *Physics of Plasmas* **29** 032512 (*Preprint* https://doi.org/10.1063/5.0080785) URL https://doi.org/10.1063/5.0080785
[15] Hölllig K 2003 *Finite Element Methods with B-Splines* (Society for Industrial and Applied Mathematics (SIAM))
[16] DeBoor C 1987 *A Practical Guide to Splines, Applied Mathematical Sciences* vol vol 27 (Springer)
[17] Jolliet S, Bottino A, Angelino P, Hatzky R, Tran T, Mcmillan B, Sauter O, Appert K, Idomura Y and Villard L 2007 *Computer Physics Communications* **177** 409 – 425 ISSN 0010-4655 URL http://www.sciencedirect.com/science/article/pii/S0010465507002251
[18] Bottino A, Vernay T, Scott B, Brunner S, Hatzky R, Jolliet S, McMillan B F, Tran T M and Villard L 2011 *Plasma Physics and Controlled Fusion* **53** 124027 URL https://doi.org/10.1088%2F0741-3335%2F53%2F12%2F124027
[19] Donnel P, Gheller C, Brunner S, Villard L, Lanti E, Ohana N and Murugappan M 2020 *Plasma Physics and Controlled Fusion* **63** 025006 URL https://doi.org/10.1088/1361-6587/abc92b
[20] Tronko N, Bottino A and Sonnendruecker E 2016 *Physics of Plasmas* **23** 082505 (*Preprint* https://doi.org/10.1063/1.4960039) URL https://doi.org/10.1063/1.4960039
[21] Bottino A and Sonnendrücker E 2015 *J. Plasma Phys.* **81** 435810501 URL https://doi.org/10.1017/s0022377815000574
[22] Mishchenko A, Bottino A, Biancalani A, Hatzky R, Hayward-Schneider T, Ohana N, Lanti E, Brunner S, Villard L, Borchardt M, Kleiber R and Koenies A 2018 *Computer Physics Communications* ISSN 0010-4655 URL http://www.sciencedirect.com/science/article/pii/S0010465518304181

[23] Hatzky R, Kleiber R, Könies A, Mishchenko A, Borchardt M, Bottino A and Sonnendrücker E 2019 *Journal of Plasma Physics* **85** 905850112
[24] Lauber P *et al.* 2018 Strongly nonlinear energetic particle dynamics in asdex-upgrade scenarios with core impurity accumulation *27th IAEA Fusion Energy Conference (Proc. 27th IAEA FEC)* (https://conferences.iaea.org/event/151/contributions/6094/)
[25] Novikau I, Biancalani A, Bottino A, Lauber P, Poli E, Manz P, Conway G D, Di Siena A, Ohana N, Lanti E and Villard L 2020 *Phys. Plasmas* **27** URL https://doi.org/10.1063/1.5142802
[26] Vannini F, Biancalani A, Bottino A, Hayward-Schneider T, Lauber P, Mishchenko A, Poli E, Vlad G and Team A U 2021 *Phys. Plasmas* **28** URL https://doi.org/10.1063/5.0049588
[27] Rettino B, Hayward-Schneider T, Biancalani A, Bottino A, Lauber P, Chavdarovski I, Weiland M, Vannini F and Jenko F 2022 *Nuclear Fusion* **62** 076027 URL https://doi.org/10.1088/1741-4326/ac6680
[28] Vannini F, Biancalani A, Bottino A, Hayward-Schneider T, Lauber P, Mishchenko A, Poli E, Rettino B, Vlad G and Wang X 2022 *Nuclear Fusion* URL http://iopscience.iop.org/article/10.1088/1741-4326/ac8b1e
[29] Vlad G, Wang X, Vannini F, Briguglio S, Carlevaro N, Falessi M V, Fogaccia G, Fusco V, Zonca F, Biancalani A, Bottino A, Hayward-Schneider T and Lauber P 2021 *Nuclear Fusion* **61** 116026 URL https://doi.org/10.1088/1741-4326/ac2522